

## Additive laser excitation of giant nonlinear surface acoustic wave pulses

Jude Deschamps<sup>1</sup>, Yun Kai<sup>1</sup>, Jet Lem<sup>1,2</sup>, Ievgeniia Chaban<sup>1</sup>, Alexey Lomonosov<sup>3</sup>, Abdelmadjid Anane<sup>4</sup>, Steven E. Kooi<sup>2</sup>, Keith A. Nelson<sup>1,2</sup> and Thomas Pezeril<sup>1,5,\*</sup>


<sup>1</sup>*Department of Chemistry, Massachusetts Institute of Technology, Cambridge, Massachusetts 02139, USA*

<sup>2</sup>*Institute for Soldier Nanotechnologies, Massachusetts Institute of Technology, Cambridge, Massachusetts 02139, USA*

<sup>3</sup>*B+W Department, Offenburg University of Applied Sciences, 77652 Offenburg, Germany*

<sup>4</sup>*Unité Mixte de Physique CNRS/Thales, UMR CNRS 137, 91767 Palaiseau, France*

<sup>5</sup>*Institut de Physique de Rennes, UMR CNRS 6251, Université Rennes 1, 35042 Rennes, France*

 (Received 29 September 2022; revised 17 August 2023; accepted 28 August 2023; published 17 October 2023)

The technique of laser ultrasonics perfectly meets the need for noncontact, noninvasive, nondestructive mechanical probing of nanometer- to millimeter-size samples. However, this technique is limited to the excitation of low-amplitude strains, below the threshold for optical damage of the sample. In the context of strain engineering of materials, alternative optical techniques enabling the excitation of high-amplitude strains in a nondestructive optical regime are needed. We introduce here a nondestructive method for laser-shock wave generation based on additive superposition of multiple laser-excited strain waves. This technique enables strain generation up to mechanical failure of a sample at pump laser fluences below optical ablation or melting thresholds. We demonstrate the ability to generate nonlinear surface acoustic waves (SAWs) in Nb-SrTiO<sub>3</sub> substrates, with associated strains in the percent range and pressures up to 3 GPa at 1 kHz repetition rate and close to 10 GPa for several hundred shocks. This study paves the way for the investigation of a host of high-strain SAW-induced phenomena, including phase transitions in conventional and quantum materials, plasticity and a myriad of material failure modes, chemistry and other effects in bulk samples, thin layers, and two-dimensional materials.

DOI: [10.1103/PhysRevApplied.20.044044](https://doi.org/10.1103/PhysRevApplied.20.044044)

### I. INTRODUCTION

Surface acoustic waves (SAWs) involving nanometer-scale atomic motion are used with routine, low-power operation in a plethora of microelectronic devices [1]. The confinement of strain near the sample surface and propagation over millimeter distances make SAWs attractive for a wide range of applications. Typically, these megahertz-frequency waves are coherently generated and detected by interdigital transducers (IDTs) deposited on a piezoelectric layer or substrate. Though well-established IDT SAW techniques are limited by small strain amplitudes, it is already possible to employ them to tune material properties [1–5]. Reaching much higher SAW strain amplitudes, up to the mechanical failure of a sample, would open up a wide range of novel applications. Until now, pulsed lasers have been used to generate high-amplitude nonlinear SAW shocks with strain amplitudes in the percent range and pressures in the 1–10 GPa range [6–11], but only operating on a single-shot basis because optical damage to the

irradiated sample region which occurs even if the shock itself does not cause damage where it propagates.

Large static strains of several percent can be applied to bulk or thin samples up to the onset of plasticity or fracture [12–16]. However, since kinetic effects can lead to distinct differences from quasi-static behavior, approaches capable of generating fast actuation mechanisms to explore material responses to dynamic strain are of keen interest. For that purpose, laser-based methods for generation of shock waves have been developed for the study of samples under intense dynamic strain loading. In the most common configuration, bulk shock waves are studied, sometimes nondestructively from femtosecond lasers with a maximum pressure in the 1 GPa range [17–21], but most often destructively in the nanosecond regime with pressures reaching tens of GPa [22–26]. Optical damage imposes severe restrictions including a very limited number of shots on a sample of small size or in a specialized environment such as a cryostat, poor shot-to-shot reproducibility for samples that are not uniform from one region to the next, and no possibility of many measurements on the same sample region in order to explore cumulative effects of repeated moderate shock loading.

\*Corresponding author. [pezeril@mit.edu](mailto:pezeril@mit.edu)

Here, we present a methodology for the excitation of nondestructive nonlinear SAWs in Nb-SrTiO<sub>3</sub> substrates, at high repetition rate, limited only by the mechanical strength of the sample. Our technique for the excitation of nonlinear strains in the percent range is based on the spatiotemporal superposition of numerous laser-excited nanosecond strain waves for SAW amplification. Fundamentally, we demonstrate a different way to achieve nonlinear acoustics. Instead of using a single high-amplitude strain wave already in the nonlinear regime, we demonstrate linear superposition of many weak strain waves to build up a shock wave in a solid. Additionally, we present a femtosecond defocusing imaging technique that can adequately reveal with great sensitivity the nonlinear reshaping of the propagative SAW.

## II. RESULTS AND DISCUSSIONS

### A. Gigahertz pulse train excitation

Various configurations enabling the spatiotemporal tailoring of laser sources for acoustic wave generation in the megahertz frequency range have been explored in the past, ranging from a moving laser source [27] to an array of synchronized lasers [28,29] and the use of a white cell to split an input laser beam [30]. The current approach borrows the general idea while simplifying the required experimental apparatus. The setup used in this study employs a free-space angular-chirp-enhanced delay (FACED) cavity [31], depicted in Fig. 1(a), whose purpose is to split an input pulsed laser beam (300 ps pulse duration, 1 kHz repetition rate) into a train of subpulses spread in time and space. The device consists of two slightly angled high-reflective planar mirrors separated by a distance  $d$  corresponding to an interpulse time separation  $\tau \approx 2d/c$ , where  $c$  is the

speed of light. In this work,  $d$  is about 30 cm, corresponding to an interpulse time separation  $\tau$  of 2 ns. Since the train of pulses exiting the FACED device are angularly dispersed, each output beam of the pulse train can be focused to a separate location on the sample surface, as depicted schematically in Fig. 1(b). An array of line sources is obtained at the sample surface, as shown on the image of Fig. 1(c). See Appendix A for the full optical schematic.

Each individual line gets absorbed in the opaque material, inducing a thermoelastic response. This process launches acoustic waves that propagate in the vicinity of the surface, namely a SAW and a surface-skimming longitudinal wave (SSLW), moving at the Rayleigh wave velocity  $v_R$  and longitudinal wave velocity  $v_L$ , respectively. By tuning the tilt angle  $\alpha$  of the FACED cavity, the line spacing  $\Delta x$  can be finely scanned until the spatiotemporal spread matches the propagation velocity of either wave. Note that the tilt angles are so small (in the milliradian range) that tuning them does not substantially modify the interpulse delay  $\tau$ . At specific angles  $\alpha$ , the coherent superposition of all the individual acoustic waves leads to the buildup of a large-amplitude wave in the phase-matched direction. The surface displacement  $u_z$  induced by the passage of the acoustic waves is monitored through reflective interferometric probing [32] using two optical probes located on both sides of the excitation region [see Fig. 1(c)].

In order to demonstrate the effectiveness of the acoustic amplification platform, we performed experiments on Nb-doped SrTiO<sub>3</sub> substrates (Nb-STO). The Nb-STO substrates (0.7% wt Nb) were purchased from MTI Corporation. No additional coatings were deposited on the substrates. SrTiO<sub>3</sub> is among the most common substrates for sample deposition, and as such could be used in the study of strain-induced effects in materials that are either

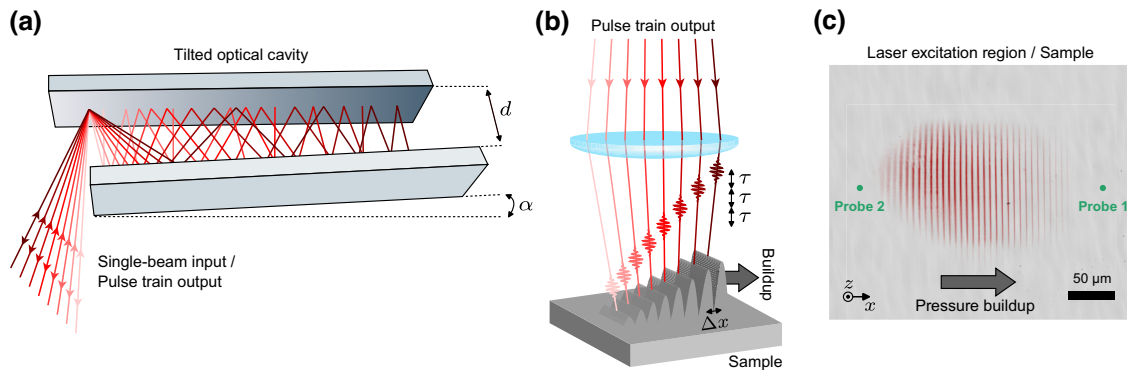


FIG. 1. Schematic representation of the platform. (a) A pulsed laser beam, focused by a cylindrical lens into a tilted optical cavity, generates a pulse train with a temporal separation  $\tau = 2d/c$ , in the nanosecond range. (b) The pulse train is focused on the sample surface; each laser pulse is laterally displaced by an amount  $\Delta x$  to match the propagation of the acoustic wave generated. The lateral displacement is fine-tuned by adjusting the mirror misalignment angle  $\alpha$ . (c) Representative time-integrated image of the sample surface, showing the laser excitation profile of the pulse train and the locations of the two interferometric probes.

deposited as exfoliated two-dimensional (2D) layers or grown as thin films on the substrates. Figures 2(a) and 2(b) show typical waveforms acquired from the Nb-STO sample for parameters tuned to amplify either the SAW moving at the Rayleigh wave velocity  $v_R$  or the SSLW moving at the longitudinal wave velocity  $v_L$ . See Appendix B for the acoustic resonances of the SAW and SSLW. Note that the additive amplified wave is detected at the probe 1 location, and non-phase-matched waves, traveling in the opposite direction, are recorded by probe 2 [see Fig. 1(c)]. The large amplified SAW pulse is very prominent as compared to the tiny ripples that come from all the individual SAWs traveling in the opposite direction. The SSLW is significantly amplified as well, but, since the interferometric detection is sensitive to the surface displacement which is perpendicular to the longitudinal displacement, it is hidden in the SAW ripples.

The significant amplitudes of the SAWs observed in our study result from a Nb doping level of approximately 0.7%, which yields a penetration depth of about 15  $\mu\text{m}$  for the 800-nm pump pulses. An exponentially decaying thermoelastic stress with this depth corresponds well with the depth-dependent SAW profile.

### B. Multiple pulse, single pulse, and ring excitation

A comparison of SAW generation in the current multiline method to a single-line approach is shown in Fig. 2(c). Very high interferometric displacements  $u_z$  of around 100 nm, and corresponding in-plane strain amplitudes  $u_{x,x} = 0.01$ , can be reached using the multiline approach with a Nb-STO substrate. As shown on the left vertical scale of Fig. 2(c), strain amplitudes of 1.0% can be attained at a 1 kHz repetition rate, with strains up to 3.0% observed in the finite-shot regime—when the total number of shots

is limited to several hundred before SAW-induced damage to Nb-STO occurs. Importantly, multiline excitation in the finite-shot regime enables the onset of plasticity to be reached before any optical damage is induced from the pump laser light in the irradiated region, which is not the case for single-line excitation that results in optical damage at about 20 times lower strain amplitude.

High strain amplitudes can alternatively be achieved through the use of a circular (“ring”) excitation geometry, which enables acoustic amplification through focusing. For comparison with the multiline approach, we have performed ring shock experiments on Nb-STO substrates under the same experimental conditions described previously [22] with a ring diameter of 160  $\mu\text{m}$ . For a given fluence, strain amplitudes about three times higher can be attained with the multiline 1D geometry compared to the 2D ring geometry [see Fig. 2(c)]. The current 1D planar scheme simplifies the interpretation of the data since the strain is unidirectional and there is no acoustic divergence or sudden change of phase from focusing.

### C. Shock-induced mechanical damage without optical damage

In the fluence range from 1.1 to 2.6  $\text{J cm}^{-2}$  that corresponds to the plastic regime, repetitive laser shots, of the order of several hundred, lead to mechanical failure from cumulative fatigue. Figure 3(a) shows a post-shock confocal microscopy image of a Nb-STO surface taken following an experiment in the plastic regime, at a pump fluence of 1.1  $\text{J cm}^{-2}$ . The laser excitation sequence was interrupted after 3000 laser shots/SAW shocks, before the mechanical damage reached the excitation region. Fractured regions with significant material ejection (see inset)

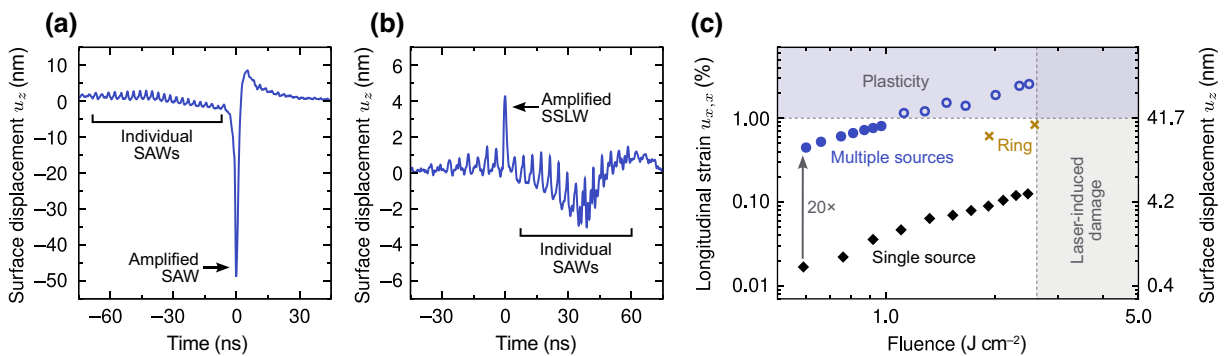


FIG. 2. Time traces of the interferometric displacements  $u_z$  and corresponding calculated in-plane strains  $u_{x,x}$ . (a) Amplification of the SAW for a Nb-STO sample, at 1.0  $\text{J cm}^{-2}$  laser fluence. (b) Same as (a) but for a SSLW. (c) Comparison of the current multiline approach (blue circles) to a single-line generation scheme (black diamonds). On Nb-STO, the multiline approach generates SAWs that can bring the material into the plastic regime (empty circles), with mechanical failure occurring from cumulative fatigue. The range of surface displacements and corresponding strains achievable can be extended by lowering the repetition rate of SAW generation, from the 1 kHz rate (full circles) to the finite-shot regime (empty circles). A comparison to the ring shock geometry [22] with a 160  $\mu\text{m}$  diameter circular pattern of pump laser light is also shown (crosses). The colored regions denote the regimes where mechanical and/or optical damage is observed on the sample.

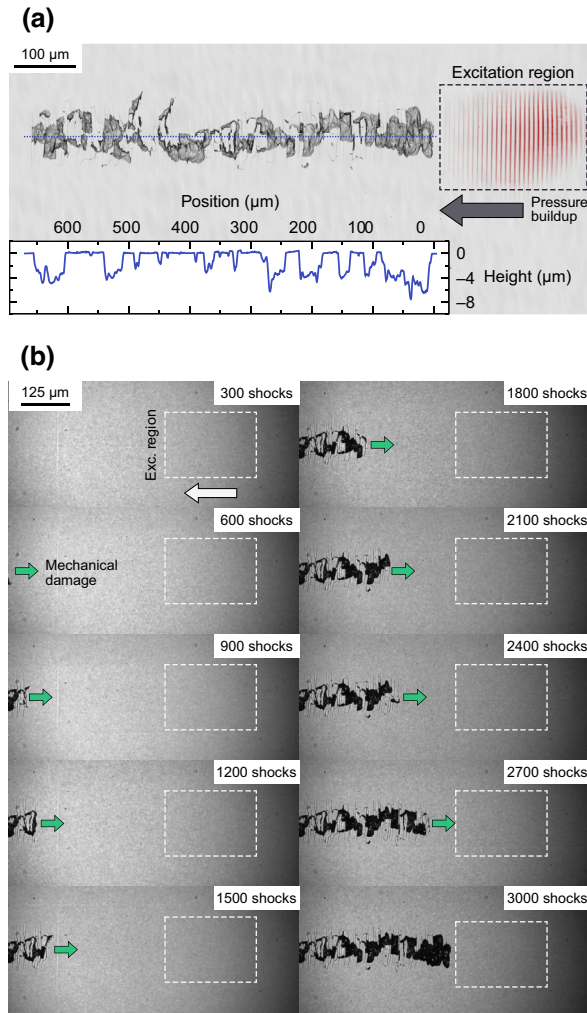


FIG. 3. Shock-induced mechanical damage without optical damage. (a) Confocal image of the surface of a Nb-STO(100) sample showing SAW-induced mechanical damage hundreds of micrometers away from the laser-excitation region. The SAW propagated along the [010] direction. Inset: depth profile along the dotted line. (b) Snapshots of SAW-induced damage on Nb-STO(100) after various numbers of laser shots/ SAW shocks. It takes about 3000 laser shots for the mechanical damage to spread to the laser-excitation region.

as well as fine deformation features along the [100] crystallographic direction can be seen a few hundreds of micrometers away from the nondamaged pump region, in the direction of propagation of the amplified SAWs.

In order to monitor the evolution of the SAW-induced mechanical damage on a Nb-STO(100) sample, we have used a femtosecond light pulse to record instantaneous snapshot images of the sample surface following laser excitation. The laser fluence of the pulse train was set to  $1.1 \text{ J cm}^{-2}$  and the laser repetition rate was lowered to 100 Hz for these experiments. As shown in Fig. 3, snapshot images obtained at intervals of 300 pump shots reveal that after about 600 shots, the damaged region becomes visible

within the camera's field of view, and it eventually reaches the excitation region after 3000 shots. Mechanical damage initially occurred at a location millimeters away from the excitation region, out of the camera field of view, with subsequent shots progressively inducing fractures closer to the excitation region. More detailed analysis of repeated SAW-induced damage will be presented in a subsequent publication.

It is worth emphasizing that a substantial number of shots, in the thousands range, is necessary to induce mechanical alterations on the sample surface in the immediate vicinity of the laser excitation region. This particular region is of considerable importance since a material deposited onto the STO surface could be tested for its behavior under repeated high strains without any optical irradiation. A submicron deposited layer would undergo the same (purely longitudinal) strains as the free STO surface.

#### D. Nonlinear SAW observation at 1 kHz and modeling

The onset of plasticity and mechanical failure from the multiline scheme can be explained by analyzing the nonlinear evolution of the SAWs as they propagate. High-amplitude waves will develop a steepening shock front with increasing peak stress as they propagate due to the elastic nonlinearity of the medium [6,33–35]. The nonlinear SAW reshaping can be revealed by techniques sensitive to a spatial derivative of the waveform, such as Schlieren imaging or the shadowgraph technique [36]. In this work, a simple transient reflectivity setup with a slightly defocused imaging system has been used to probe the SAW temporal evolution. Figure 4(a) shows a series of snapshots of the Nb-STO(111) sample surface, recorded using a 400-nm femtosecond probe pulse as the illumination source. The direction of propagation was chosen to be  $[\bar{1}12]$  to maximize the elastic nonlinearity [8,37]. The contrast  $\Delta R/R$  in the transient reflectivity maps of Fig. 4(a) stems from two contributions, namely the photoelastic effect [38] and Fresnel diffraction from propagation of the optical field over the defocus length  $\Delta z$ . The latter effect has been analyzed before in the context of phonon-polariton and quasi-bulk shock imaging [39–41]. For small propagation lengths of the optical field, it is most sensitive to the Laplacian of the surface displacement:

$$\frac{\Delta R}{R} \propto -\frac{\lambda \Delta z}{2\pi} \nabla^2 u_z(x, y), \quad (1)$$

with  $\lambda$  the probe wavelength. The contribution of defocusing to the measured contrast can reach tens of percent, dominating over the photoelastic contribution, easily revealing the location and shape of the acoustic wave. The predominant effect of the Fresnel diffraction has been further confirmed experimentally from the fact that the

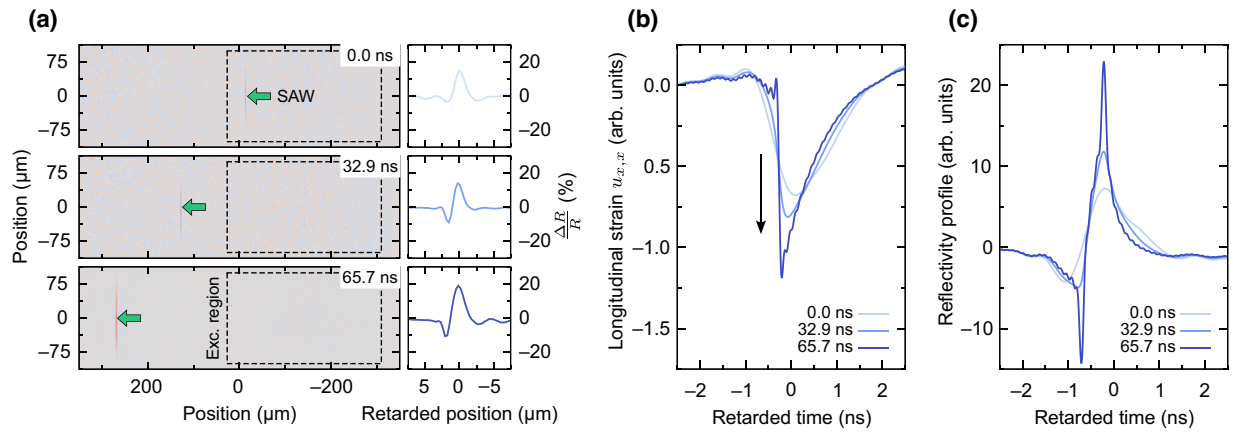


FIG. 4. Nonlinear reshaping of the SAW. (a) Time-resolved femtosecond reflectivity images for SAWs traveling along the  $[1\bar{1}2]$  direction of a Nb-STO(111) sample. An arrow points to the SAW location in each frame. The excitation region is outlined with a dashed box. Profiles extracted from a cut of the reflectivity maps along the horizontal dimension are shown on the right. (b) Numerical modeling of the longitudinal strain  $u_{x,x}$  that matches the experimental observations in (a). The arrow shows the increase in peak strain as the wave propagates. (c) Corresponding simulated optical reflectivity profiles.

reflectivity contrast switches sign when the defocus length  $\Delta z$  is reversed.

From the evolution of the reflectivity imaging data taken as the SAW moves away from the excitation region, shown in Fig. 4(a), we experimentally observe the reshaping of the SAW profile. The data show a significant growth of the positive reflectivity image peak and of the negative peak, initially absent at 0.0 ns (this time is taken as the time the amplified SAW leaves the excitation region). Particularly notable here is the experimental observation of the nonlinear reshaping of GPa-level SAWs in a repetitive and nondestructive manner. It demonstrates the possibility of averaging repetitive multishot experiments in the nonlinear regime. Previously, the observation of Rayleigh shock waves had been limited to single-shot experiments [6–9]. The implementation of a kilohertz repetition rate method holds great promise for significantly enhancing the signal-to-noise ratio of the collected data when shock-induced damage does not occur and for characterization of cumulative nanoscale shock effects (applying x-ray imaging or other high-resolution methods after different numbers or amplitudes of shocks) prior to macroscopic material failure when it does occur.

Numerical simulations were performed in order to understand the experimentally observed nonlinear evolution of Fig. 4(a). The simulation basically consists of propagating nonlinearly an acoustic waveform. The initial acoustic waveform is given by an experimentally measured interferometric displacement profile like the one in Fig. 2(a). See Appendix C for a short summary of the numerical simulations, the results of which are shown in Fig. 4(b). These simulations allow us to draw some conclusions on the nonlinear reshaping of the SAW in-plane strain  $u_{x,x}$ . Initially, as expected from the thermoelastic excitation

process [42], the strain profile is purely compressive (there is no tensile strain component). This differs from the ablative process for which the strain profile is bipolar (tensile strain followed by compressive strain). Then, as the SAW propagates nonlinearly, the compressive strain component grows significantly in amplitude due to nonlinear reshaping. Note that in terms of strain-engineering applications, it can be convenient to load samples with high-amplitude unipolar strains and not a mix of positive and negative strains whose effects are more complex to disentangle. The projection of the stress along particular slip systems eventually reaches the yield stress of the material, which explains how fracture first appears significantly distant from the excitation region when the pump fluence is set just above the onset of plasticity. Figure 4(c) shows the second derivative of the calculated surface displacement profile, qualitatively matching the evolution of the reflectivity profiles shown in Fig. 4(a), which further confirms the capture of nonlinear dynamics from time-resolved imaging reflectivity measurements. Note that the simulation in Fig. 4(c) shows a sharper shock front than the results in Fig. 4(a) because of the limited spatial resolution of our optical measurements.

### III. CONCLUSION AND PERSPECTIVES

This work establishes a versatile nondestructive technique for the generation of high-amplitude SAW strains in solid substrates. Notably, Nb-STO substrates, commonly used for sample deposition, make it possible to reach SAW strain amplitudes of more than 1.0% (up to 3.0% or 10 GPa in the finite-shot regime) before any type of damage—mechanical or laser-induced—occurs. The current technique enables transduction of high amplitude SAWs into samples of interest deposited on the substrates, and

will thereby facilitate the study of dynamic strain effects in a wide range of materials. Additionally, the large surface displacements reached using the current platform enable the use of a simple transient reflectivity imaging technique to track linear or nonlinear acoustic wave evolution in materials. Extension of this work to bulk compressional waves will be possible with less strongly absorbing samples including STO with a lower Nb doping concentration for reduced absorption of the pump light. More uniform light absorption (e.g., optical penetration depth of 100  $\mu\text{m}$  or more) will produce a thermoelastic stress that will drive a primarily compressional bulk-like shock, as we have seen for shock generation with single intense pulses in the single-shot regime [22]. Additionally shear acoustic waves are generally very difficult to efficiently laser-excite [43], especially to reach large strain amplitudes. The excitation of Stoneley or Scholte surface-interface waves [44], between Nb-STO and thick solid or viscoelastic liquid materials using the present technique, could enable strong shear strain loading and the study of shear degrees of freedom in disordered or ordered systems including supercooled liquids and glasses, mixed ferroelectrics and multiferroics, magnetic materials and others. Finally, other materials besides STO may show capacities for nondestructive generation of stronger surface or bulk shocks and for longer or even indefinite resilience against failure at higher strains, enabling robust systems for repeated transduction of shocks in studies of shock responses and fatigue mechanisms in many materials.

## ACKNOWLEDGMENTS

We acknowledge insightful discussions with Alexei Maznev from MIT, Andreas Mayer from Offenburg University, Kevin Tsia from the University of Hong Kong, as well as Takakazu Suzuki, visiting student at MIT from Keio University. The MIT experimental work of J.D. and K.A.N. was supported by the U.S. Department of Energy, Office of Basic Energy Sciences, under Award No. DE-SC0019126. J. L. and Y. K. acknowledge support from the U.S. Army through the Institute for Soldier Nanotechnologies under Contract ARO69680-18 with the U.S. Army Research Office. S. E. K. acknowledges funding from the DEVCOM Soldier Center and the Assistant Secretary of the Army for Acquisition Logistics and Training, specifically 0601102A Defense Sciences. T.P. acknowledges financial support from Direction Générale de l'Armement (DGA) under Grant No. ERE 2017 60 0040 as well as from Région Bretagne under grant SAD. Y.K. acknowledges support from a German Academic Exchange Service (DAAD) fellowship.

## APPENDIX A: OPTICAL SETUP

### 1. Pump path

The pump pulse is derived from the uncompressed output of a 1 kHz Ti-sapphire regenerative amplifier

(Coherent Astrella) with a central wavelength of 800 nm and pulse duration of 300 ps full width at half maximum (FWHM). Up to 1.6 mJ of pulse energy is used as input for the tilted optical cavity. A half-wave plate and polarizing beam-splitter combination is used as a variable attenuator to adjust the pump energy. The pump beam is focused by a cylindrical lens near the back mirror of the cavity in order to enter the cavity with a wide range of wavevector components along the cavity direction. The beam propagates back and forth through the cavity, and reemerges at the entrance location in the form of multiple beams at successive wavevector components among those of the incident beam. The beams with successively higher wavevector components emerge from the cavity after successively increased numbers of round-trips in the cavity. Consequently, the output of the cavity is a spatiotemporally spaced pulse train with an interpulse separation equal to the round-trip time of the cavity. The output beams are reflected by a beamsplitter and are directed toward the sample. A second cylindrical lens (orthogonal to the first) is used to form an array of lines at the microscope objective focus, which coincides with the sample surface location.

### 2. Probe path

The probe beam is derived from a continuous-wave frequency-doubled Nd-YAG (Coherent Verdi) laser operating at a central frequency of 532 nm with an average power at the sample of less than 10 mW. The laser output is diffracted by a transmissive binary phase mask. The optical field at the phase mask location is then relayed to the back focal plane of the objective lens of a Keplerian 2-lens telescope; a beam block is placed at the Fourier plane of the telescope to filter out all diffraction orders besides the  $\pm 1$  orders. The probes are focused on the sample on each side of the excitation region, as shown in Fig. 1(c). Their reflections are recombined interferometrically at the same phase mask [32], and the intensity of the signal beam is detected using a fast avalanche photodiode (Hamamatsu APD C5658) connected to a high-bandwidth oscilloscope. As the amplified surface waves propagate through probe 1, the sample surface displacement  $u_z$  induces an optical path difference  $\xi = 2u_z$  between both arms of the interferometer, which is translated into a change of intensity  $I$  of the signal beam,

$$I(\xi) = \langle I \rangle \left[ 1 - V \sin \left( \frac{2\pi\xi}{\lambda} + \phi_0 \right) \right], \quad (\text{A1})$$

where  $\langle I \rangle$  is the average intensity,  $V$  is the interferometric visibility,  $\lambda$  is the probe wavelength, and  $\phi_0 \in [-\pi, \pi]$  is the phase offset of the interferometer. The phase offset can be tuned at the highest sensitivity point by horizontal translation of the phase mask.

### 3. Transient reflectivity imaging path

Transient reflectivity imaging capabilities are available to the setup. The compressed output of the Ti:sapphire regenerative amplifier (Coherent Astrella), with a pulse duration of about 90 fs FWHM, is frequency-doubled to 400 nm in a beta barium borate crystal. A set of variable-length fibers is then used to variably delay the pulse propagation. The beam is finally used as an expanded illumination source on the sample, and its reflection is collected on a CMOS sensor (Hamamatsu Orca Flash). The acquisition of each active frame (with the acoustic wave) is followed by the acquisition of a reference frame (without the acoustic wave).

### 4. Fluence calibration

The fluence axis in Fig. 2(c) is calibrated using the following procedure. For each data point, the total laser pulse energy that is delivered to the sample is measured. This value is then divided by the total effective area covered by the multiline or single-line excitation pattern. Note that the effective area of each line is defined by the product of the FWHM values of its Gaussian intensity profile along the length and width directions.

### APPENDIX B: ACOUSTIC PHASE MATCHING

Each individual pump line focused on the sample gets absorbed in the material, inducing a thermoelastic response. This process launches acoustic waves that propagate in the vicinity of the surface, namely a surface acoustic wave and a surface-skimming longitudinal wave moving at the Rayleigh wave velocity  $v_R$  and longitudinal wave velocity  $v_L$ , respectively. By tuning the tilt angle  $\alpha$  of the FACED cavity, the line spacing can be finely scanned until the spatiotemporal spread matches the propagation velocity of either wave. Note that the tilt angles are so small (in the milliradian range) that tuning them does not substantially modify the interpulse delay  $\tau$ . At specific angles  $\alpha$ , the coherent superposition of individual acoustic waves leads to the buildup of a large-amplitude wave in the phase-matched direction. Figure 6 shows two resonances obtained from scanning the line spacing  $\Delta x$  of the excitation pattern experimentally performed by tuning the angle  $\alpha$  of the cavity, corresponding to the selective amplification of a SAW or a SSLW. The plotted quantities are the FWHM durations and amplitudes of the interferometrically measured signal peaks like those shown in Figs. 2(a) and 2(b). When the line spacing is optimized for either wave, the wave components generated at all the lines are superposed and the duration of the amplified wave is minimized. When the line spacing is not optimal, the temporal superposition of the wave components generated at all the lines is not optimized, and the different components arrive at the Probe 1 location (see Fig. 1(c)) at somewhat different

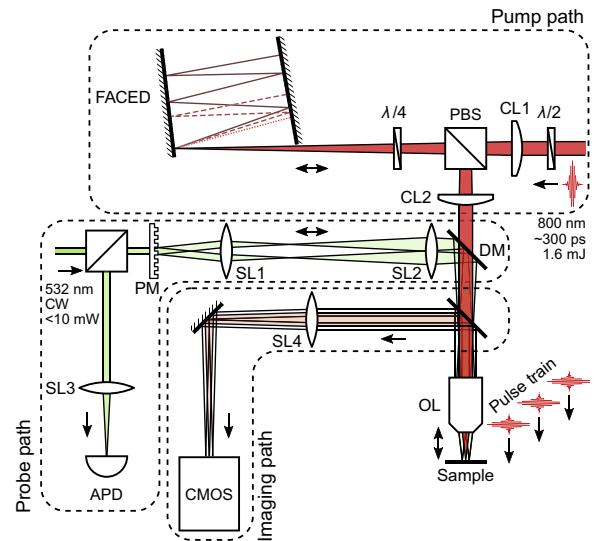


FIG. 5. Schematic illustration of the platform.  $\lambda/2$ , half-wave plate; CL1, cylindrical lens 1 ( $f = 500$  mm); PBS, polarizing beam splitter;  $\lambda/4$ , quarter-wave plate; FACED, free-space angular-chirp-enhanced delay device; CL2, cylindrical lens 2 ( $f = 500$  mm); DM, dichroic mirror; OL, objective lens (Mitutoyo M Plan Apo 10 $\times$ ); PM, binary phase mask; SL1, spherical lens 1 ( $f = 100$  mm); SL2, spherical lens 2 ( $f = 175$  mm); SL3, spherical lens 3 ( $f = 100$  mm); APD, avalanche photo-diode (Hamamatsu C5658); SL4, spherical lens 4 ( $f = 400$  mm); CMOS, complementary metal oxide semiconductor sensor (Hamamatsu ORCA).

times, resulting in an amplified wave with longer FWHM duration and lower peak amplitude. In some cases it may be of interest to determine material responses including fatigue effects with different strain durations. The Rayleigh

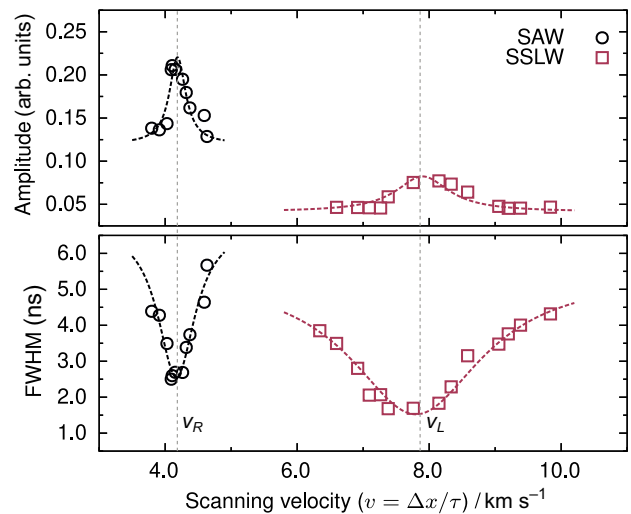


FIG. 6. Acoustic resonances obtained on Nb-STO from scanning the line spacing  $\Delta x$  of the excitation pattern. Dotted lines are guides to the eye.

velocity and longitudinal velocity of the waves can be extracted from the positions of the FWHM peak minima, which correspond as well to the amplitude maxima.

### APPENDIX C: NUMERICAL SIMULATIONS

As a SAW pulse propagates across a nonlinear elastic medium, its shape changes gradually due to nonlinear distortion. Within the quadratic approximation and assuming the nonlinear distortion is slow (in the sense that the change over a distance comparable with the pulse width is small), the nonlinear evolution can be understood as an interaction among the Fourier components that results in the generation of sum and difference frequencies. Quantitatively, this process is described by the evolution equation system derived previously [45]:

$$i \frac{d}{d\tau} B_n = n v_R \left[ \sum_{m=0}^n F(m/n) B_m B_{n-m} + 2 \sum_{m=n}^{\infty} (n/m) F^*(n/m) B_m B_{m-n}^* \right]. \quad (\text{C1})$$

Here,  $v_R$  is the Rayleigh velocity,  $B_n$  is the  $n$ th Fourier component of the Rayleigh wave strain profile,  $\tau$  is the propagation distance, and the function  $F$  characterizes the rate of harmonics generation.

The experimental waveform measured interferometrically at a location close to the source is expanded in the Fourier series and fed to the evolution system of equations as the initial condition. The system is integrated numerically over the propagation distance, and finally the inverse Fourier transform gives the predicted waveform. The kernel function  $F$  depends on the second- and third-order elastic constants of the solid, and on the geometry of the problem if the solid is anisotropic. All the constants used

TABLE I. Parameters used for the numerical simulations in Nb-STO.

	SrTiO <sub>3</sub>
$\rho / \text{kg m}^{-3}$	5175
$C_{11} / \text{GPa}$	294
$C_{12} / \text{GPa}$	102
$C_{44} / \text{GPa}$	116
$C_{111} / \text{GPa}$	-4960
$C_{112} / \text{GPa}$	-770
$C_{123} / \text{GPa}$	20
$C_{144} / \text{GPa}$	-810
$C_{166} / \text{GPa}$	-300
$C_{456} / \text{GPa}$	90
$v_R$ along $[\bar{1}12] / \text{m s}^{-1}$	4129
$ F(1/2) $	0.6276

for the simulations, such as the second- and third-order elastic constants of Nb-STO [46,47], are listed in Table I.

- [1] P. Delsing, A. N. Cleland, M. J. A. Schuetz, J. Knörzer, G. Giedke, J. I. Cirac, K. Srinivasan, M. Wu, K. C. Balram, and C. Bäuerle, *et al.*, The 2019 surface acoustic waves roadmap, *J. Phys. D: Appl. Phys.* **52**, 353001 (2019).
- [2] W.-G. Yang and H. Schmidt, Acoustic control of magnetism toward energy-efficient applications, *Appl. Phys. Rev.* **8**, 021304 (2021).
- [3] M. Foerster, F. Macià, N. Statuto, S. Finizio, A. Hernández-Mínguez, S. Lendínez, P. V. Santos, J. Fontcuberta, J. M. Hernández, and M. Kläui, *et al.*, Direct imaging of delayed magneto-dynamic modes induced by surface acoustic waves, *Nat. Commun.* **8**, 407 (2017).
- [4] F. Iikawa, A. Hernández-Mínguez, I. Aharonovich, S. Nakhaie, Y.-T. Liou, J. M. J. Lopes, and P. V. Santos, Acoustically modulated optical emission of hexagonal boron nitride layers, *Appl. Phys. Lett.* **114**, 171104 (2019).
- [5] R. Fandan, J. Pedrós, A. Hernández-Mínguez, F. Iikawa, P. V. Santos, A. Boscá, and F. Calle, Dynamic local strain in graphene generated by surface acoustic waves, *Nano Lett.* **20**, 402 (2020).
- [6] A. Lomonosov, V. G. Mikhalevich, P. Hess, E. Y. Knight, M. F. Hamilton, and E. A. Zabolotskaya, Laser-generated nonlinear Rayleigh waves with shocks, *J. Acoust. Soc. Am.* **105**, 2093 (1999).
- [7] A. M. Lomonosov and P. Hess, Impulsive fracture of silicon by elastic surface pulses with shocks, *Phys. Rev. Lett.* **89**, 095501 (2002).
- [8] A. M. Lomonosov, P. Hess, R. E. Kumon, and M. F. Hamilton, Laser-generated nonlinear surface wave pulses in silicon crystals, *Phys. Rev. B* **69**, 035314 (2004).
- [9] A. M. Lomonosov and P. Hess, Nonlinear surface acoustic waves: Realization of solitary pulses and fracture, *Ultrasonics* **48**, 482 (2008).
- [10] D. Veysset, A. Maznev, I. Veres, T. Pezeril, S. Kooi, A. Lomonosov, and K. Nelson, Acoustical breakdown of materials by focusing of laser-generated Rayleigh surface waves, *Appl. Phys. Lett.* **111**, 031901 (2017).
- [11] D. Veysset, S. Kooi, R. Haferssas, M. Hassani-Gangaraj, M. Islam, A. Maznev, Y. Chernukha, X. Zhao, K. Nakagawa, D. Martynowich, *et al.*, Glass fracture by focusing of laser-generated nanosecond surface acoustic waves, *Scripta Materialia* **158**, 42 (2019).
- [12] R. Xu, J. Huang, E. S. Barnard, S. S. Hong, P. Singh, E. K. Wong, T. Jansen, V. Harbola, J. Xiao, and B. Y. Wang, *et al.*, Strain-induced room-temperature ferroelectricity in SrTiO<sub>3</sub> membranes, *Nat. Commun.* **11**, 3141 (2020).
- [13] S. Hameed, D. Pelc, Z. W. Anderson, A. Klein, R. J. Spieker, L. Yue, B. Das, J. Ramberger, M. Lukas, and Y. Liu, *et al.*, Enhanced superconductivity and ferroelectric quantum criticality in plastically deformed strontium titanate, *Nat. Mater.* **21**, 54 (2021).
- [14] D. G. Schlom, L.-Q. Chen, C. J. Fennie, V. Gopalan, D. A. Muller, X. Pan, R. Ramesh, and R. Uecker, Elastic strain engineering of ferroic oxides, *MRS Bull.* **39**, 118 (2014).



- [15] D. Yu, J. Feng, and J. Hone, Elastically strained nanowires and atomic sheets, *MRS Bull.* **39**, 157 (2014).
- [16] S. Dhole, A. Chen, W. Nie, B. Park, and Q. Jia, Strain engineering: A pathway for tunable functionalities of perovskite metal oxide films, *Nanomaterials* **12**, 835 (2022).
- [17] P. J. van Capel and J. I. Dijkhuis, Optical generation and detection of shock waves in sapphire at room temperature, *Appl. Phys. Lett.* **88**, 151910 (2006).
- [18] A. Bojahr, D. Schick, L. Maerten, M. Herzog, I. Vrejoiu, C. K. Schmising, C. Milne, S. L. Johnson, and M. Bargheer, Comparing the oscillation phase in optical pump-probe spectra to ultrafast x-ray diffraction in the metal-dielectric SrRuO<sub>3</sub>/SrTiO<sub>3</sub> superlattice, *Phys. Rev. B* **85**, 224302 (2012).
- [19] V. V. Temnov, C. Klieber, K. A. Nelson, T. Thomay, V. Knittel, A. Leitenstorfer, D. Makarov, M. Albrecht, and R. Bratschitsch, Femtosecond imaging of nonlinear acoustics in gold, *Nat. Commun.* **4**, 1468 (2013).
- [20] T. Pezeril, C. Klieber, V. Shalagatskyi, G. Vaudel, V. Temnov, O. Schmidt, and D. Makarov, Femtosecond imaging of nonlinear acoustics in gold, *Opt. Express* **22**, 4590 (2014).
- [21] C. Klieber, V. Gusev, T. Pezeril, and K. A. Nelson, Nonlinear acoustics at GHz frequencies in a viscoelastic fragile glass former, *Phys. Rev. Lett.* **114**, 065701 (2015).
- [22] T. Pezeril, G. Saini, D. Veyssset, S. Kooi, P. Fidkowski, R. Radovitzky, and K. A. Nelson, Direct visualization of laser-driven focusing shock waves, *Phys. Rev. Lett.* **106**, 214503 (2011).
- [23] G. Morard, S. Boccato, A. D. Rosa, S. Anzellini, F. Miozzi, L. Henry, G. Garbarino, M. Mezouar, M. Harmand, and F. Guyot, *et al.*, Solving controversies on the iron phase diagram under high pressure, *Geophys. Res. Lett.* **45**, 11,074 (2018).
- [24] S. B. Brown, A. E. Gleason, E. Galtier, A. Higginbotham, B. Arnold, A. Fry, E. Granados, A. Hashim, C. G. Schroer, and A. Schropp, *et al.*, Direct imaging of ultrafast lattice dynamics, *Sci. Adv.* **5**, eaau8044 (2019).
- [25] E. E. McBride, A. Krygier, A. Ehnes, E. Galtier, M. Harmand, Z. Konôpková, H. J. Lee, H.-P. Liermann, B. Nagler, and A. Pelka, *et al.*, Phase transition lowering in dynamically compressed silicon, *Nat. Phys.* **15**, 89 (2019).
- [26] F. Li and D. D. Dlott, High throughput tabletop shock techniques and measurements, *J. Appl. Phys.* **131**, 075901 (2022).
- [27] Y. H. Berthelot and I. J. Busch-Vishniac, Thermoacoustic radiation of sound by a moving laser source, *J. Acoust. Soc. Am.* **81**, 317 (1987).
- [28] M. Noroy, D. Royer, and M. Fink, The laser-generated ultrasonic phased array: Analysis and experiments, *J. Acoust. Soc. Am.* **94**, 1934 (1993).
- [29] T. W. Murray, J. B. Deaton, and J. W. Wagner, Experimental evaluation of enhanced generation of ultrasonic waves using an array of laser sources, *Ultrasonics* **34**, 69 (1996).
- [30] J. B. Deaton and J. W. Wagner, Variable-cavity-length mode-locked Nd:YAG laser for noncontact generation and spectral control of narrow-band ultrasound, *Appl. Opt.* **33**, 1051 (1994).
- [31] J.-L. Wu, Y.-Q. Xu, J.-J. Xu, X.-M. Wei, A. C. Chan, A. H. Tang, A. K. Lau, B. M. Chung, H. C. Shum, and E. Y. Lam, *et al.*, Ultrafast laser-scanning time-stretch imaging at visible wavelengths, *Light Sci. Appl.* **6**, e16196 (2016).
- [32] C. Glorieux, J. D. Beers, E. H. Bentefour, K. Van de Rostyne, and K. A. Nelson, Phase mask based interferometer: Operation principle, performance, and application to thermoelastic phenomena, *Rev. Sci. Instrum.* **75**, 2906 (2004).
- [33] N. Kalyanasundaram, R. Ravindran, and P. Prasad, Coupled amplitude theory of nonlinear surface acoustic waves, *J. Acoust. Soc. Am.* **72**, 488 (1982).
- [34] D. F. Parker, Waveform evolution for nonlinear surface acoustic waves, *Int. J. Eng. Sci.* **26**, 59 (1988).
- [35] M. F. Hamilton, Y. A. Il'inskii, and E. A. Zabolotskaya, Nonlinear surface acoustic waves in crystals, *J. Acoust. Soc. Am.* **105**, 639 (1999).
- [36] G. S. Settles, *Schlieren and Shadowgraph Techniques* (Springer, Berlin Heidelberg, 2001).
- [37] P. Hess and A. M. Lomonosov, Nanotechnological applications of nonlinear surface acoustic waves: Mechanism of brittle fracture, *Appl. Surf. Sci.* **248**, 123 (2005).
- [38] H. Yamazaki, O. Matsuda, and O. B. Wright, Surface phonon imaging through the photoelastic effect, *Phys. Status Solidi C* **1**, 2991 (2004).
- [39] R. M. Koehl, S. Adachi, and K. A. Nelson, Direct visualization of collective wavepacket dynamics, *J. Phys. Chem. A* **103**, 10260 (1999).
- [40] B. Sitalakshmi, A. Vudayagiri, S. Sreedhar, and N. Viswanathan, On-axis time-resolved spatial characterization of shock-induced refractive fringes in liquid water, *J. Opt. Soc. Am. B* **30**, 2206 (2013).
- [41] L. Dresselhaus-Cooper, J. Gorfain, C. Key, B. Ofori-Okai, S. Ali, D. Martynowich, A. Gleason, S. Kooi and K. Nelson, Single-shot multi-frame imaging of cylindrical shock waves in a multi-layered assembly, *Sci. Rep.* **9**, 3689 (2019).
- [42] C. B. Scruby and L. E. Drain, *Laser Ultrasonics, Techniques and Applications* (Taylor & Francis Group, New York, 1990).
- [43] T. Pezeril, Laser generation and detection of ultrafast shear acoustic waves in solids and liquids, *Opt. Laser Technol.* **83**, 177 (2016).
- [44] C. Glorieux, K. Van de Rostyne, J. Goossens, G. Shkerdin, W. Lauriks, and K. A. Nelson, Shear properties of glycerol by interface wave laser ultrasonics, *J. Appl. Phys.* **99**, 013511 (2006).
- [45] C. Eckl, A. S. Kovalev, A. P. Mayer, A. M. Lomonosov, and P. Hess, Solitary surface acoustic waves, *Phys. Rev. E* **70**, 046604 (2004).
- [46] R. W. Lardner and G. E. Tupholme, Nonlinear surface waves on cubic materials, *J. Elasticity* **16**, 251 (1986).
- [47] H. Yang and W. Q. Huang, Theoretical predication method of high order elastic constants of cubic and tetragonal crystal material, *Adv. Mater. Res.* **834-836**, 263 (2013).